Simulating inplane fatigue damage in woven glass fibre-reinforced composites subject to fully-reversed cyclic loading

W. VAN PAEPEGEM[*] and J. DEGRIECK

Ghent University, Dept. of Mechanical Construction and Production, Sint-Pietersnieuwstraat 41, B-9000 Gent, Belgium

ABSTRACT The interest for use of fibre-reinforced composites in structural components is increasing. Some of these structural composites, such as wind turbine blades, aircraft components and torsion shafts are subject to fatigue loadings.

It is widely accepted that fully-reversed cyclic loading is the most adverse loading for fibre-reinforced composites, but the modelling of the material behaviour under this loading condition is very difficult. In this paper a damage model is presented for woven glass fibre-reinforced composites subject to fully-reversed cyclic loading. First fatigue experiments have been conducted in displacement-controlled fully-reversed bending and the stiffness degradation and damage patterns have been observed. Based on these experimental data, a damage model has been developed which includes the inplane stress components and the degradation of the inplane elastic properties. The model has been implemented in a commercial finite element code and simulation of the successive stages in fatigue life has been performed.

The model has been validated for a plain woven glass fabric reinforced composite and simulated stiffness degradation, damage growth and damage distribution have been compared with experimental data.

Keywords fatigue; composites; residual stiffness; tension-compression.

NOMENCLATURE

c_i (i = 1,...,9)	material constants for glass/epoxy material
C_{ij}	homogenized stiffness tensor of the undamaged material
D_{ij} (i, j = 1,2)	in-plane damage variables
d_{11}^t	tensile damage related with positive stress σ_{11}
d_{11}^c	compressive damage related with negative stress σ_{11}
d_{22}^t	tensile damage related with positive stress σ_{22}
d_{22}^c	compressive damage related with negative stress σ_{22}
d_{12}^+	shear damage related with positive stress σ_{12}

[*] Corresponding author (Fax: +32-(0)9-264.35.87, E-mail: Wim.VanPaepegem@UGent.be).

d_{12}^-	shear damage related with negative stress σ_{12}
E_{11}	stiffness modulus in warp direction of the glass/epoxy lamina
E_{22}	stiffness modulus in weft direction of the glass/epoxy lamina
ε_{ij}	strain tensor
ε_{ii}^p (i = 1,2)	permanent strain
h	crack closure coefficient
N	number of cycles
R	stress ratio (= $\sigma_{min}/\sigma_{max}$)
R_d	displacement ratio (= u_{min}/u_{max})
S	shear strength of glass/epoxy lamina
σ_{ij}	stress tensor
$\widetilde{\sigma}_{ij}$	two-dimensional effective stresses ($\widetilde{\sigma}_{ij} = \sigma_{ij}/(1-D_{ij})$)
Σ_{ij} (i, j = 1,2)	in-plane fatigue failure indices
u_{max}	maximum prescribed displacement in bending fatigue setup
X_T	tensile strength in warp direction of glass/epoxy lamina
X_C	compression strength in warp direction of glass/epoxy lamina
Y_T	tensile strength in weft direction of glass/epoxy lamina
Y_C	compression strength in weft direction of glass/epoxy lamina
[#0°]₈	stacking sequence of eight glass/epoxy laminae, the weft direction being aligned with the loading direction in bending
[#45°]₈	stacking sequence of eight glass/epoxy laminae, the weft (and warp) direction under 45° with the loading direction in bending

INTRODUCTION

The use of fibre-reinforced composites in fatigue-critical structural components is growing steadily. Wind turbine blades, helicopter blades, aircraft wings,... are subject to cyclic loadings during service life. The fatigue behaviour of fibre-reinforced composites is quite different from the one exposed by metals. Composites are made of reinforcing fibres embedded in a polymer matrix and are therefore heterogeneous and anisotropic. Fatigue damage can start very early, after only a few or a few hundred loading cycles. This first stage of degradation consists of a multitude of microscopic cracks and other forms of damage, such as debonding and pull-out of fibres from the matrix. The elastic properties of the material, in particular the stiffness, are affected by this fatigue damage and are gradually decreasing. Due to the stiffness degradation, load is transferred from damaged areas to neighbouring undamaged areas and hence stress redistribution occurs. In a latter stage more serious types of damage appear, such as fibre breakage and unstable delamination growth, leading to an accelerated decline and final failure.

For fully-reversed cyclic loading, the applied stress amplitude changes sign during one fatigue loading cycle. It has been often reported in literature that this sign reversal of the applied stress has a detrimental effect on fatigue life [1-5]. In multi-directional laminates, the plies, with and without fibres in the loading direction, develop intraply damage, and this causes local delamination at relatively short lifetimes. In tensile loading this is less serious, as the plies containing fibres aligned with the loading direction, continue to support the majority of the applied load. In compression, however, tensile-induced damage can lead to local instability and buckling, perhaps before resin and interfacial damage within the plies initiate fibre microbuckling [6].

Even if no delaminations are present, Gamstedt and Sjögren [5] observed that the total length of transverse cracks grew to be more than twice as large for tension-compression fatigue compared to tension-tension fatigue. They explained that, when a debond is subjected to compressive loading, an opening zone appears at the tips of the interfacial crack. Since debond propagation is more susceptible to mode I loading, the debond growth rate will be larger in compression. Indeed, for global tension, crack propagation would be in pure shear mode because the crack tip is closed.

Recently, a *one-dimensional* damage model for *fully-reversed cyclic loading* was proposed by the authors [7]. The Continuum Damage Mechanics theory [8-14] and the residual stiffness approach [15-17] were the basis for the model. Damage growth, residual stiffness and stress redistribution were predicted by the model. The formulation was applied to fully-reversed cyclic loading of unidirectional laminates which was considered as a one-dimensional loading case.

The same approach was used to develop a *multi-dimensional* damage model for *non-reversed cyclic loading* [7,18]. In that model, all inplane stress components σ_{11}, σ_{22} and σ_{12} were considered, but only for non-reversed cyclic loading.

In this paper, features of both cited damage models will be integrated into a *multi-dimensional* model for *fully-reversed cyclic loading*, where the stress state is two-dimensional and both normal stresses and shear stresses are applied to the material. First, the experimental results will be discussed. Next a short review of the one-dimensional damage model for fully-reversed cyclic loading and the multi-dimensional damage model for non-reversed cyclic loading will be presented. These models will then be extended for two-dimensional stress states. Finally the results of the finite element simulations will be shown.

EXPERIMENTAL SETUP AND MATERIALS

Experimental setup

The experimental results were obtained from displacement-controlled cantilever bending fatigue experiments. One side of the specimen was clamped, while a sinusoidal displacement was imposed at the other side of the specimen. Figure 1 shows a schematic drawing.
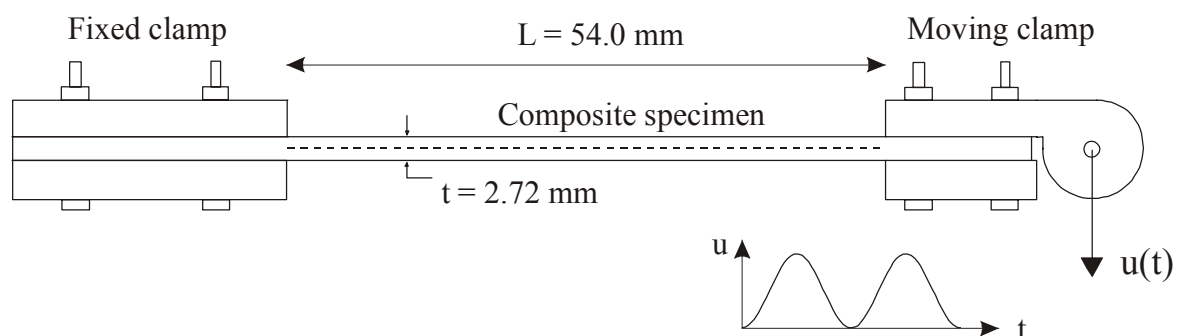

Figure 1   **Schematic drawing of the bending fatigue setup.**

The displacement amplitude u_{max} can be adjusted by the controlling mechanism. An additional parameter is the displacement ratio $R_d = \dfrac{u_{min}}{u_{max}}$ (analogous to the stress ratio R), where u_{min} and u_{max} are evaluated with their algebraic signs. If $R_d = 0.0$, the fatigue test is performed in single-sided bending, while it is performed in fully-reversed bending if $R_d = -1.0$; i.e. the deflection can vary from zero to the maximum deflection in one direction, or in two opposite directions, respectively.

Uni-axial fatigue experiments in tension/compression are most often used in fatigue research [19-21] and accepted as a standard fatigue test, while bending fatigue experiments are not used so frequently to study the fatigue behaviour of composites [22-24]. Nevertheless bending fatigue experiments were preferred to uni-axial tension/compression fatigue tests because of the following reasons:

- the bending moment is (piecewise) linear along the length of the specimen (3-point bending, 4-point bending, cantilever beam bending). Hence stresses, strains and damage distribution vary along the gauge length of the specimen. On the contrary, with tension/compression fatigue experiments, the stresses, strains and damage are assumed to be equal in each cross-section of the specimen,

- in uni-axial tension/compression fatigue tests, buckling poses serious problems while in fully-reversed bending tests this problem is overcome.

- the finite element implementation gives rise to several complications, because each material point is loaded with a different stress, strain and possibly stress ratio, so that damage growth can be different for each material point. In uni-axial tension/compression fatigue tests, the stress- or strain-amplitude is constant during fatigue life and differential equations describing decrease of stiffness or strength, can often be simply integrated over the considered number of loading cycles. Hence, the fatigue damage model resulting from bending fatigue tests should be more general in use and thus more suited for modelling full-scale structural composite components,

- smaller forces and larger displacements in bending allow a more slender design of the fatigue testing facility.

These reasons favoured the decision to use a bending fatigue setup instead of a tensile fatigue setup.

Material

The material was an epoxy matrix with a plain woven glass fabric. The warp direction of all eight layers made up an angle of 45° with the bending direction (denoted as [#45°]$_8$, where the hash mark '#' refers to the fabric reinforcement type). The bending of the [#45°]$_8$ stacking sequence results in a combined state of normal stresses in the two fibre directions of the fabric, and shear stresses.

For the one-dimensional model, the stacking sequence [#0°]$_8$ was used, where the warp direction of all eight layers has been aligned with the bending direction. The bending of the [#0°]$_8$ stacking sequence results in a quasi one-dimensional loading of the laminate, with large stresses along the longitudinal fibre direction.

Figure 2 shows that both stacking sequences exhibit a quite different behaviour in fully-reversed bending ($R_d = -1.0$). The force amplitude necessary to bend the specimen into its maximum deformed state, is initially higher for the [#0°]$_8$ specimen, but decreases very fast.

The $[\#45°]_8$ shows a large initial decline as well, but then the degradation is much more gradual.

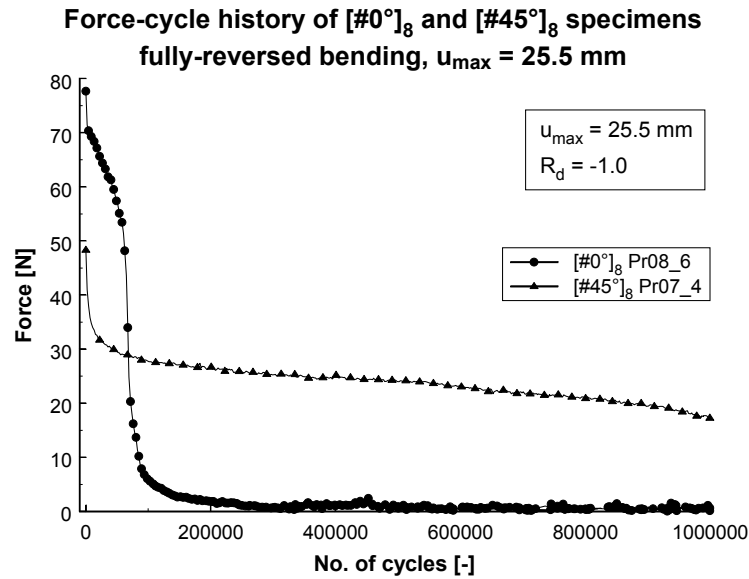**Figure 2**   **Force-cycle histories for $[\#0°]_8$ and $[\#45°]_8$ specimens (fully-reversed bending R_d = -1.0, u_{max} = 25.5 mm).**

The one-dimensional model [7] aimed at simulating the fatigue behaviour of the $[\#0°]_8$ specimens, while the extended model will predict the fatigue behaviour of the $[\#45°]_8$ specimens.
Next a short review of the *one-dimensional* damage model for *fully-reversed cyclic loading* and the *multi-dimensional* damage model for *non-reversed cyclic loading* will be presented.

ONE-DIMENSIONAL MODEL FOR FULLY-REVERSED CYCLIC LOADING

The complete derivation of the constitutive equations can be found in reference [7]. Here only the outline of the model is recalled.

During one fatigue loading cycle, the one-dimensional stress σ changes sign. Its maximum value in tension is supposed to contribute to the "tensile" damage d_{11}^t, while its maximum value in compression is causing "compressive" damage d_{11}^c. These damage variables d_{11}^t and d_{11}^c are assumed to represent the effect of the underlying physical damage mechanisms on the macroscopic stiffness property E_{11}, if pure zero-tension or zero-compression loading would be applied in the direction $\vec{e}_{11}$. As such, the model for fully-reversed cyclic loading can reduce to its equivalent for non-reversed cyclic loading if either zero-tension or zero-compression loading is applied.
In 1971, Lemaitre [25] introduced the concept of strain equivalence which states that a damaged volume of material under the nominal stress σ shows the same strain response as a comparable undamaged volume under the effective stress $\tilde{\sigma}$. Following the Continuum

Damage Mechanics theory and the work of Lemaitre [10,25], the effective stress $\tilde{\sigma}$ was defined in this work as:

$$\tilde{\sigma} = \frac{\sigma}{1-(d_{11}^t + d_{11}^c)} \quad \text{if } \sigma \geq 0$$
$$\tilde{\sigma} = \frac{\sigma}{1-(d_{11}^c + h\,d_{11}^t)} \quad \text{if } \sigma < 0$$

(1)

where h is a crack closure coefficient which characterizes the closure of the micro-cracks and micro-cavaties in compression. This closure coefficient h can be calculated from the measurement on the damaged material of the elasticity modulus in tension $E_t = E \cdot (1-D)$ and the elasticity modulus in compression $E_c = E \cdot (1-hD)$. Its value was set to 0.2 [7,10].

To introduce the strength properties of the material into the equations, the fatigue failure index Σ was defined as the ratio of the effective stress $\tilde{\sigma}$ (which includes the fatigue damage) to the static strength:

$$\Sigma = \frac{\tilde{\sigma}}{X} \qquad \begin{cases} X = X_T & \text{if } \sigma \geq 0 \\ X = -|X_C| & \text{if } \sigma < 0 \end{cases}$$

(2)

It is important to note that through this definition, the fatigue failure index Σ becomes a function of σ, d_{11}^t and d_{11}^c.

The accelerated growth rate in fully-reversed cyclic loading was modelled by coupling the differential equations for $d(d_{11}^t)/dN$ and $d(d_{11}^c)/dN$. The final system of damage growth rate equations was written as [7]:

$$
\begin{cases}
\begin{aligned}
\frac{d(d_{11}^t)}{dN} = & \; c_1 \cdot \left(1+\left(d_{11}^c\right)^2\right) \cdot \Sigma \cdot \exp\left(-c_2 \frac{d_{11}^t}{\sqrt{\Sigma} \cdot \left(1+\left(d_{11}^c\right)^2\right)}\right) & \text{if } \sigma \geq 0 \\
& + c_3 \cdot d_{11}^t \cdot \Sigma^2 \cdot \left[1 + \frac{\sqrt{d_{11}^c} \exp\left(c_8 \sqrt{d_{11}^c}\right)}{1+\exp\left(-c_5(\Sigma-c_7)\right)}\right] \cdot \left[1+\exp\left(c_5(\Sigma-c_4)\right)\right] \\[2em]
\frac{d(d_{11}^c)}{dN} = & \; \left[c_1 \cdot \left(1+\left(d_{11}^t\right)^2\right) \cdot \Sigma \cdot \exp\left(-c_2 \frac{d_{11}^c}{\sqrt{\Sigma} \cdot \left(1+\left(d_{11}^t\right)^2\right)}\right)\right]^{1+2\cdot\exp\left(-c_6 \cdot d_{11}^t\right)} & \text{if } \sigma < 0 \\
& + c_3 \cdot d_{11}^c \cdot \Sigma^2 \cdot \left[1 + \frac{\sqrt{d_{11}^t} \exp\left(c_8 \sqrt{d_{11}^t}\right)}{1+\exp\left(-c_5(\Sigma-c_7)\right)}\right] \cdot \left[1+\exp\left(\frac{c_5}{3}(\Sigma-c_4)\right)\right]
\end{aligned} \\
D_{11} = d_{11}^t + d_{11}^c
\end{cases}
$$

(3)

For the maximum tensile stress ($\sigma > 0$) in the fatigue loading cycle, the fatigue failure index Σ is calculated and the damage growth rate $d(d_{11}^t)/dN$ is calculated. Next, the maximum compressive stress ($\sigma < 0$) in the fatigue loading cycle leads to a damage growth rate $d(d_{11}^c)/dN$. Both differential equations have two terms, the first term accounting for damage initiation and the second term accounting for damage propagation and final failure. The material constants c_i (i=1,...,8) each have a clear physical meaning and five of them (c_1 through c_5) can be calculated from single-sided bending tests [18,26]. Indeed, c_1 and c_2

account for the damage initiation, while c_3, c_4 and c_5 account for damage propagation in non-reversed cyclic loading The constant c_6 expresses the experimental observation that damage initiation in the compressive regime is accelerated by the presence of tensile damage, as reported by Gamstedt and Sjögren [5]. The constants c_7 and c_8 are introduced in the damage propagation function, which simulates that once the fatigue failure index Σ has crossed the threshold c_7, the damage propagation is accelerated because of the presence of the other damage type (d_{11}^t or d_{11}^c).

Now, as the *one-dimensional* model for *fully-reversed cyclic loading* has been reviewed, the *multi-dimensional* model for *non-reversed cyclic loading* will be discussed.

MULTI-DIMENSIONAL MODEL FOR NON-REVERSED CYCLIC LOADING

For the non-reversed cyclic loading tests, the experimental material was the $[\#45°]_8$ glass/epoxy laminate. It was observed that considerable permanent deformation occurred during the bending fatigue tests (setup see Figure 1). So the model should be able to simulate: (i) stiffness degradation (decreasing bending force), (ii) stress redistribution, and (iii) accumulation of permanent strain.

To that purpose, a residual stiffness model was developed with three damage variables: D_{11} (damage in the $\vec{e}_{11}$ direction), D_{22} (damage in the $\vec{e}_{22}$ direction), and D_{12} (shear damage). These damage variables are directly related with the corresponding stress components σ_{11} (positive/negative), σ_{22} (positive/negative) and σ_{12} in the orthotropic directions of the glass/epoxy composite. For each of the three damage variables, the growth rate per fatigue cycle N is defined by a differential equation $d(D_{ij})/dN$. To make a prediction of the moment of failure, the governing stresses σ_{11}, σ_{22} and σ_{12} in the corresponding differential equations have been replaced by the defined *fatigue failure indices* Σ_{11}, Σ_{22} en Σ_{12}. These failure indices are calculated from the Tsai-Wu static failure criterion, where the nominal stresses σ_{11}, σ_{22}, and σ_{12} are replaced by the effective stresses $\tilde{\sigma}_{11}$, $\tilde{\sigma}_{22}$ and $\tilde{\sigma}_{12}$ (the effective stresses are defined here as $\tilde{\sigma}_{ij} = \sigma_{ij}/(1 - D_{ij})$). As such, there is a correlation with residual strength, and the moment of failure in the displacement-controlled bending fatigue tests can be predicted as well. Finally, the permanent strains ε_{ii}^p (i=1,2) have been introduced. The growth rate $d(\varepsilon_{ii}^p)/dN$ is proportional with the strain ε_{ii} and the growth rate $d(D_{12})/dN$.

A detailed derivation of the modelling framework can be found in reference [27] and [28]. Here the relevant equations are summarized.

Relevant equations

Three relationships make up the complete modelling framework: (i) the damage-stiffness relationships, (ii) the fatigue damage evolution laws $d(D_{ij})/dN$, and (iii) the growth laws for the permanent strains ε_{ii}^p. These three relationships are discussed in the following paragraphs.

Damage-stiffness relationships

It is first postulated that there is a distinct difference between the damage kinetics of intra-layer damage (matrix cracks, fibre/matrix debonding, fibre fracture,…) and inter-layer damage (delaminations). Moreover the responsible stress components are not the same. The

inplane stresses (σ_{11}, σ_{22} and σ_{12}) are affecting the intra-layer damage, while the out-of-plane stresses (σ_{13}, σ_{23} and σ_{33}) are causing inter-layer damage. It is clear that the one-dimensional fatigue damage model developed so far, is modelling the intra-layer damage types. Delaminations were not taken into account and the stacking sequence was chosen such that delaminations did not develop under the experimental loading conditions.

If only intra-layer damage is considered, it is *postulated* that there exist three damage variables D_{11}, D_{22} and D_{12}, which are defined through the relations:

$$
\begin{Bmatrix} \sigma_{11} \\ \sigma_{22} \\ \sigma_{33} \\ \sigma_{23} \\ \sigma_{13} \\ \sigma_{12} \end{Bmatrix} =
\begin{bmatrix}
\sqrt{1-D_{11}} & 0 & 0 & 0 & 0 & 0 \\
0 & \sqrt{1-D_{22}} & 0 & 0 & 0 & 0 \\
0 & 0 & 1 & 0 & 0 & 0 \\
0 & 0 & 0 & 1 & 0 & 0 \\
0 & 0 & 0 & 0 & 1 & 0 \\
0 & 0 & 0 & 0 & 0 & \sqrt{1-D_{12}}
\end{bmatrix}
\cdot
\begin{bmatrix}
C_{11} & C_{12} & C_{13} & 0 & 0 & 0 \\
C_{12} & C_{22} & C_{23} & 0 & 0 & 0 \\
C_{13} & C_{23} & C_{33} & 0 & 0 & 0 \\
0 & 0 & 0 & C_{44} & 0 & 0 \\
0 & 0 & 0 & 0 & C_{55} & 0 \\
0 & 0 & 0 & 0 & 0 & C_{66}
\end{bmatrix}
\cdot
$$

$$
\begin{bmatrix}
\sqrt{1-D_{11}} & 0 & 0 & 0 & 0 & 0 \\
0 & \sqrt{1-D_{22}} & 0 & 0 & 0 & 0 \\
0 & 0 & 1 & 0 & 0 & 0 \\
0 & 0 & 0 & 1 & 0 & 0 \\
0 & 0 & 0 & 0 & 1 & 0 \\
0 & 0 & 0 & 0 & 0 & \sqrt{1-D_{12}}
\end{bmatrix}
\cdot
\begin{Bmatrix} \varepsilon_{11}-\varepsilon_{11}^{p} \\ \varepsilon_{22}-\varepsilon_{22}^{p} \\ \varepsilon_{33} \\ 2\varepsilon_{23} \\ 2\varepsilon_{13} \\ 2\varepsilon_{12} \end{Bmatrix}
\tag{4}
$$

where [C] is the initial orthotropic stiffness matrix of the composite material. In other words, the three damage variables represent the macroscopic effect of the underlying intra-layer damage mechanisms (matrix cracks, fibre/matrix interface failure,...) onto the inplane elastic properties. The permanent strains ε_{11}^{p} and ε_{22}^{p} must account for the permanent deformation of the [#45°]$_8$ specimens. Although this Equation represents a simplified approach, it is at least manageable in terms of number of damage variables and finite element implementation, because the symmetry of the stiffness matrix [C] is guaranteed at any time during fatigue life.

A very important advantage of the formulation in Equation (4) is that the damage variables D_{11}, D_{22} and D_{12} are directly related with their respective stress components σ_{11}, σ_{22} and σ_{12}. As such, the damage growth rates dD_{11}/dN, dD_{22}/dN and dD_{12}/dN are driven by the respective stresses σ_{11}, σ_{22} and σ_{12}. Further, there is a very clear distinction between positive and negative stresses for each of the damage variables. Indeed, for each damage variable, the sign of the corresponding stress component dictates which damage growth rate equation should be used, the one for tension or the one for compression.

Equation (4) can be worked out as follows:

$$
\begin{Bmatrix} \sigma_{11} \\ \sigma_{22} \\ \sigma_{33} \\ \sigma_{23} \\ \sigma_{13} \\ \sigma_{12} \end{Bmatrix} =
\begin{bmatrix}
C_{11}\cdot(1-D_{11}) & C_{12}\cdot\sqrt{1-D_{11}}\cdot\sqrt{1-D_{22}} & C_{13}\cdot\sqrt{1-D_{11}} & 0 & 0 & 0 \\
C_{12}\cdot\sqrt{1-D_{11}}\cdot\sqrt{1-D_{22}} & C_{22}\cdot(1-D_{22}) & C_{23}\cdot\sqrt{1-D_{22}} & 0 & 0 & 0 \\
C_{13}\cdot\sqrt{1-D_{11}} & C_{23}\cdot\sqrt{1-D_{22}} & C_{33} & 0 & 0 & 0 \\
0 & 0 & 0 & C_{44} & 0 & 0 \\
0 & 0 & 0 & 0 & C_{55} & 0 \\
0 & 0 & 0 & 0 & 0 & C_{66}\cdot(1-D_{12})
\end{bmatrix}
\cdot
\begin{Bmatrix} \varepsilon_{11}-\varepsilon_{11}^{p} \\ \varepsilon_{22}-\varepsilon_{11}^{p} \\ \varepsilon_{33} \\ 2\varepsilon_{23} \\ 2\varepsilon_{13} \\ 2\varepsilon_{12} \end{Bmatrix}
\tag{5}
$$

Fatigue damage evolution laws

The final objective is the development of a set of damage growth rate equations of the form:

$$\frac{dD_{11}}{dN} = \left| \begin{array}{ll} f_1(\sigma_{ij}, D_{ij}) & \text{if } \sigma_{11} \geq 0 \\ \\ f_2(\sigma_{ij}, D_{ij}) & \text{if } \sigma_{11} < 0 \end{array} \right.$$

$$\frac{dD_{22}}{dN} = \left| \begin{array}{ll} g_1(\sigma_{ij}, D_{ij}) & \text{if } \sigma_{22} \geq 0 \\ \\ g_2(\sigma_{ij}, D_{ij}) & \text{if } \sigma_{22} < 0 \end{array} \right. \tag{6}$$

$$\frac{dD_{12}}{dN} = h(\sigma_{ij}, D_{ij})$$

Each damage growth rate equation should depend on the multi-dimensional inplane stress state σ_{ij} and the actual value of the damage variables D_{ij}. As the stress components σ_{ij} give no indication of reserve to failure, new stress measures have been developed [29]. The *fatigue failure indices* Σ_{ij}^{2D} $(i, j = 1,2)$ for generalized inplane fatigue loading can be calculated from the Tsai-Wu static failure criterion by replacing the nominal stresses σ_{ij} with the effective stresses $\sigma_{ij}/(1-D_{ij})$. The corresponding fatigue failure index Σ_{11}^{2D} for the stress component σ_{11} is defined as the positive root of the equation [29]:

$$\left(\frac{1}{X_T} - \frac{1}{|X_C|} \right) \frac{\sigma_{11}}{\Sigma_{11}^{2D} \cdot (1-D_{11})} + \left(\frac{1}{Y_T} - \frac{1}{|Y_C|} \right) \frac{\sigma_{22}}{1-D_{22}} + \frac{1}{X_T \cdot |X_C|} \left(\frac{\sigma_{11}}{\Sigma_{11}^{2D} \cdot (1-D_{11})} \right)^2$$
$$+ \frac{1}{Y_T \cdot |Y_C|} \left(\frac{\sigma_{22}}{1-D_{22}} \right)^2 + \frac{1}{S^2} \left(\frac{\sigma_{12}}{1-D_{12}} \right)^2 = 1 \tag{7}$$

The fatigue failure index Σ_{22}^{2D} for the stress component σ_{22} is defined as the positive root of the equation [29]:

$$\left(\frac{1}{X_T} - \frac{1}{|X_C|} \right) \frac{\sigma_{11}}{1-D_{11}} + \left(\frac{1}{Y_T} - \frac{1}{|Y_C|} \right) \frac{\sigma_{22}}{\Sigma_{22}^{2D} \cdot (1-D_{22})} + \frac{1}{X_T \cdot |X_C|} \left(\frac{\sigma_{11}}{1-D_{11}} \right)^2$$
$$+ \frac{1}{Y_T \cdot |Y_C|} \left(\frac{\sigma_{22}}{\Sigma_{22}^{2D} \cdot (1-D_{22})} \right)^2 + \frac{1}{S^2} \left(\frac{\sigma_{12}}{1-D_{12}} \right)^2 = 1 \tag{8}$$

Finally, the fatigue failure index Σ_{12}^{2D} for the stress component σ_{12} is defined as the positive root of the equation [29]:

$$\left(\frac{1}{X_T} - \frac{1}{|X_C|}\right)\frac{\sigma_{11}}{1-D_{11}} + \left(\frac{1}{Y_T} - \frac{1}{|Y_C|}\right)\frac{\sigma_{22}}{1-D_{22}} + \frac{1}{X_T \cdot |X_C|}\left(\frac{\sigma_{11}}{1-D_{11}}\right)^2$$
$$+ \frac{1}{Y_T \cdot |Y_C|}\left(\frac{\sigma_{22}}{1-D_{22}}\right)^2 + \frac{1}{S^2}\left(\frac{\sigma_{12}}{\Sigma_{12}^{2D} \cdot (1-D_{12})}\right)^2 = 1 \tag{9}$$

These *fatigue failure indices* Σ_{11}^{2D}, Σ_{22}^{2D} and Σ_{12}^{2D} quantify the directional reserves to failure for inplane loading conditions, taking into account the present damage state (D_{11}, D_{22}, D_{12}).

To assess the *relative importance of the separate stress components* σ_{ij} in the failure event, it is better to correlate the failure indices Σ_{ij}^{2D} $(i, j = 1,2)$ with their one-dimensional equivalent. Also, the failure indices must reduce to their one-dimensional equivalent if the other stress components are zero.

A definition which satisfies these requirements, is the following:

$$\Sigma_{11} = \frac{\Sigma_{11}^{2D}}{1 + (\Sigma_{11}^{2D} - \Sigma_{11}^{1D})}$$

$$\Sigma_{22} = \frac{\Sigma_{22}^{2D}}{1 + (\Sigma_{22}^{2D} - \Sigma_{22}^{1D})} \tag{10}$$

$$\Sigma_{12} = \frac{\Sigma_{12}^{2D}}{1 + (\Sigma_{12}^{2D} - \Sigma_{12}^{1D})}$$

The failure indices Σ_{11}^{2D}, Σ_{22}^{2D} and Σ_{12}^{2D} are calculated from the respective equations (7), (8) and (9), while the one-dimensional failure indices Σ_{11}^{1D}, Σ_{22}^{1D} and Σ_{12}^{1D} are defined as the ratio of the effective stress $\tilde{\sigma}$ to the respective static strength. So, the two-dimensional failure indices Σ_{ij}^{2D} $(i, j = 1,2)$ take into account the adverse effect of multi-dimensional loading, while the correlation with the one-dimensional ratio Σ_{ij}^{1D} $(i, j = 1,2)$ to their respective static strengths indicates the relative probability of failure along the considered direction $\vec{e}_{11}$ or $\vec{e}_{22}$. The newly defined failure indices reduce to their one-dimensional equivalent if a one-dimensional stress is applied, so the relation between one-dimensional and multi-dimensional failure indices remains consistent in use.

It is important to observe that if the stress state approaches the Tsai-Wu failure surface, not all failure indices Σ_{ij} (i, j = 1,2) will reach the failure value 1.0, because the failure indices are normalized with respect to their one-dimensional ratio Σ_{ij}^{1D} $(i, j = 1,2)$. To avoid any singularities in the equations (7), (8) and (9) during fatigue life simulation, the calculation strategy is as follows:

- if one of the failure indices Σ_{ij} (i, j = 1,2) has a high value, the corresponding damage variable D_{ij} will grow very rapidly,

- if this failure index Σ_{ij} approaches its failure value 1.0, the corresponding stress σ_{ij} is set to zero,

- in the next evaluation of the Tsai-Wu failure indices, all terms in the stress component σ_{ij} are zero.

A detailed discussion of the damage-dependent directional failure indices Σ_{ij} can be found in [29].

In the end the close feedback between experimental observations and finite element predictions has lead to the final damage growth rate equations for multi-dimensional inplane loading [28], valid for non-reversed cyclic loading:

$$
\frac{dD_{11}}{dN} = \left|
\begin{array}{ll}
\begin{aligned}
& c_1 \cdot (1 + D_{12}^2) \cdot \Sigma_{11} \cdot \exp\left(-c_2 \frac{D_{11}}{\sqrt{\Sigma_{11}} \cdot (1 + D_{12}^2)} \right) \\
& + c_3 \cdot D_{11} \cdot \Sigma_{11}^2 \cdot \left[1 + \exp(c_5(\Sigma_{11} - c_4)) \right]
\end{aligned} & \text{if } \sigma_{11} \geq 0 \\[3em]
\begin{aligned}
& \left[c_1 \cdot (1 + D_{12}^2) \cdot \Sigma_{11} \cdot \exp\left(-c_2 \frac{D_{11}}{\sqrt{\Sigma_{11}} \cdot (1 + D_{12}^2)} \right) \right]^{1 + 2 \cdot \exp(-D_{12})} \\
& + c_3 \cdot D_{11} \cdot \Sigma_{11}^2 \cdot \left[1 + \exp\left(\frac{c_5}{3}(\Sigma_{11} - c_4) \right) \right]
\end{aligned} & \text{if } \sigma_{11} < 0
\end{array}
\right.
$$

$$
\frac{dD_{22}}{dN} = \left|
\begin{array}{ll}
\begin{aligned}
& c_1 \cdot (1 + D_{12}^2) \cdot \Sigma_{22} \cdot \exp\left(-c_2 \frac{D_{22}}{\sqrt{\Sigma_{22}} \cdot (1 + D_{12}^2)} \right) \\
& + c_3 \cdot D_{22} \cdot \Sigma_{22}^2 \cdot \left[1 + \exp(c_5(\Sigma_{22} - c_4)) \right]
\end{aligned} & \text{if } \sigma_{22} \geq 0 \\[3em]
\begin{aligned}
& \left[c_1 \cdot (1 + D_{12}^2) \cdot \Sigma_{22} \cdot \exp\left(-c_2 \frac{D_{22}}{\sqrt{\Sigma_{22}} \cdot (1 + D_{12}^2)} \right) \right]^{1 + 2 \cdot \exp(-D_{12})} \\
& + c_3 \cdot D_{22} \cdot \Sigma_{22}^2 \cdot \left[1 + \exp\left(\frac{c_5}{3}(\Sigma_{22} - c_4) \right) \right]
\end{aligned} & \text{if } \sigma_{22} < 0
\end{array}
\right.
$$

$$
\frac{dD_{12}}{dN} = c_1 \cdot \Sigma_{12} \cdot \exp\left(-c_2 \frac{D_{12}}{2\sqrt{\Sigma_{12}}} \right)
\tag{11}
$$

Growth laws for permanent strains

Finally, additional equations for the growth rate of the permanent strains ε_{ii}^p (i = 1,2) must be established. The corresponding growth laws for the permanent strain have been written as (no summation convention) [28]:

$$
\frac{d\varepsilon_{ii}^p}{dN} = \left|
\begin{array}{ll}
c_6 \cdot \varepsilon_{ii} \cdot \dfrac{dD_{12}}{dN} & \text{if } \sigma_{ii} \geq 0 \\[1.5em]
0 & \text{if } \sigma_{ii} < 0
\end{array}
\right. \qquad (i = 1,2)
\tag{12}
$$

The factor c_6 has been determined such that the predicted out-of-plane displacement profile after unloading matches the experimentally recorded one for one [#45°]$_8$. This was the case

for $c_6 = 0.6$. This implies that, if the damage D_{12} reaches its failure value 1.0, the permanent strain ε_{ii}^p cannot be larger than 60 % of the total strain amplitude ε_{ii}.

Typical finite element results

One finite element simulation of the *multi-dimensional* model for *non-reversed cyclic loading* will be shown here, because this example will be compared later with the finite element results of the *multi-dimensional* model for *fully-reversed cyclic loading.*

Figure 3 shows the experimental and simulated force-cycle history of the $[\#45°]_8$ specimen Pr04_1 for a small prescribed displacement $u_{max} = 27.7$ mm under single-sided bending ($R_d = 0.0$, non-reversed cyclic loading). It is observed that the force is barely decreasing after the initiation phase.
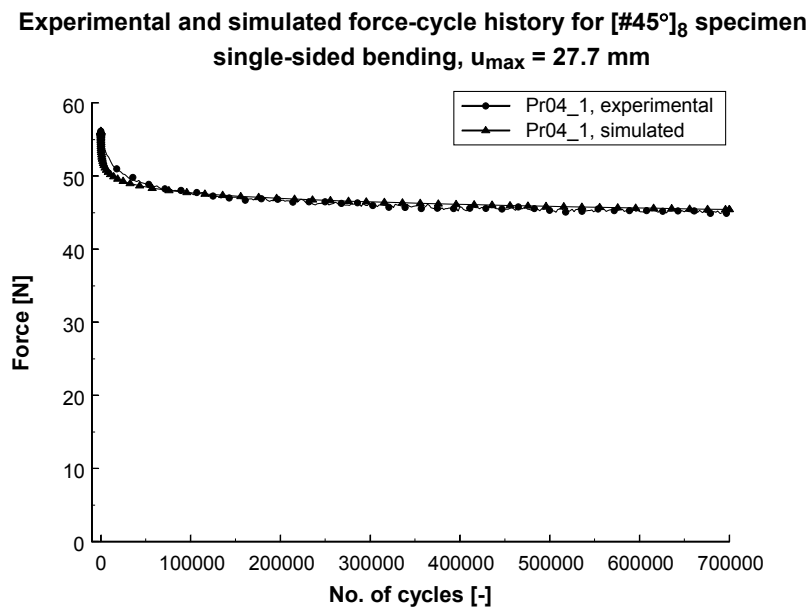

Experimental and simulated force-cycle history for $[\#45°]_8$ specimen single-sided bending, $u_{max} = 27.7$ mm

Figure 3 **Experimental and simulated force-cycle history for the $[\#45°]_8$ specimen Pr04_1 ($u_{max} = 27.7$ mm).**

This is confirmed by the predicted behaviour of the damage variables and the fatigue failure indices. Figure 4 and Figure 5 show the cycle histories of the damage variables (D_{11}, D_{22} and D_{12}) and the fatigue failure indices (Σ_{11}, Σ_{22} and Σ_{12}), respectively, for the Gauss-point 1602 (situated at the tensile surface in the clamped cross-section of the glass/epoxy specimen Pr04_1).
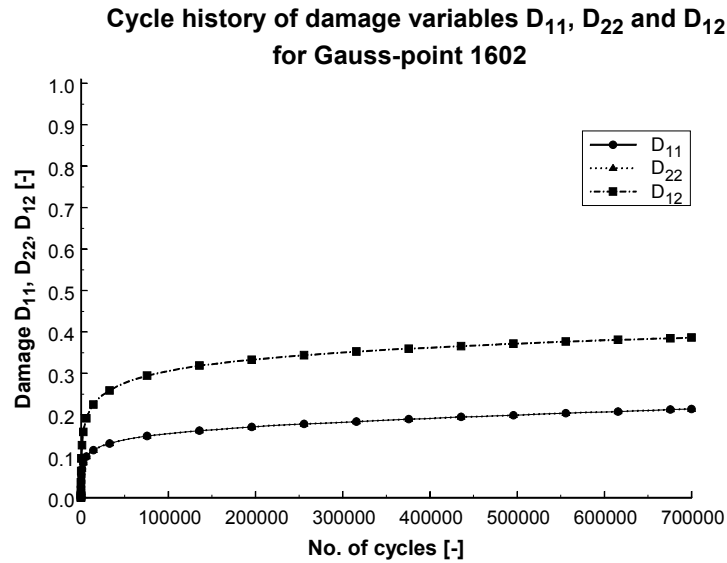
Cycle history of damage variables D₁₁, D₂₂ and D₁₂ for Gauss-point 1602

Figure 4   **Cycle history of the damage variables D_{11}, D_{22} and D_{12} for the Gauss-point 1602 ([#45°]$_8$ specimen Pr04_1, $u_{max} = 27.7$ mm).**
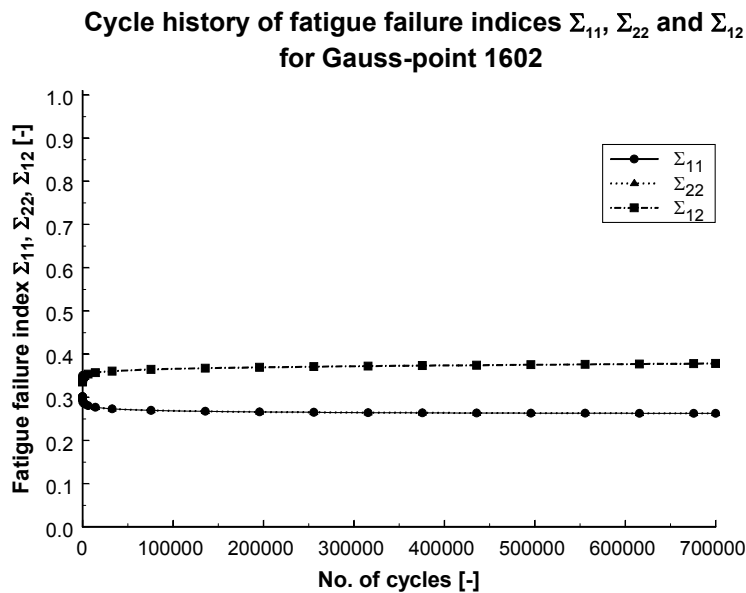
Cycle history of fatigue failure indices Σ₁₁, Σ₂₂ and Σ₁₂ for Gauss-point 1602

Figure 5   **Cycle history of the fatigue failure indices Σ_{11}, Σ_{22} and Σ_{12} for the Gauss-point 1602 ([#45°]$_8$ specimen Pr04_1, $u_{max} = 27.7$ mm).**

It can be seen that damage D_{12} reaches the highest value, compared to the damage values D_{11} and D_{22}. However, all damage variables are barely increasing after the initiation phase. The fatigue failure indices Σ_{11} and Σ_{22} even slightly decrease, due to the accumulation of permanent strain.

EXTENSION TOWARDS A MULTI-DIMENSIONAL MODEL FOR FULLY-REVERSED CYCLIC LOADING

In the previous sections, the *one-dimensional* damage model for *fully-reversed cyclic loading* and the *multi-dimensional* damage model for *non-reversed cyclic loading* have been reviewed. Now the extension will be made towards a *multi-dimensional* model for *fully-reversed cyclic loading*.

In the *one-dimensional* damage model for *fully-reversed cyclic loading*, there was made a distinction between tensile damage d_{11}^t and compressive damage d_{11}^c. The adverse effect of fully-reversed loading was modelled by coupling the differential equations $d(d_{11}^t)/dN$ and $d(d_{11}^c)/dN$.

In case of the *multi-dimensional* model for *fully-reversed cyclic loading*, the inplane stresses σ_{11}, σ_{22} and σ_{12} all change sign during one loading cycle. Similar to the one-dimensional approach for fully-reversed cyclic loading, a distinction is made between "tensile" damage d_{11}^t and "compressive" damage d_{11}^c for σ_{11}, and between "tensile" damage d_{22}^t and compressive "damage" d_{22}^c for σ_{22}. For the shear stress σ_{12}, a distinction is made between d_{12}^+ and d_{12}^-. The plus-sign and minus-sign are used because the terms "tension" and "compression" are meaningless in this context. Further, at each point of time in the fully-reversed loading cycle, the apparent stiffness of the damaged material in the compressive zone is higher than the stiffness of the damaged material in the tensile zone, due to the crack closure phenomenon (see Equation (1)). As a consequence the damage variables D_{11}, D_{22} and D_{12} are defined by the relations (no summation convention):

$$\begin{cases} D_{ii} = \begin{vmatrix} d_{ii}^t + d_{ii}^c & \text{if } \sigma_{ii} \geq 0 \\ d_{ii}^c + h\,d_{ii}^t & \text{if } \sigma_{ii} < 0 \end{vmatrix} & (i = 1, 2) \\ D_{12} = d_{12}^+ + d_{12}^- \end{cases} \tag{13}$$

If the definitions (13) are respected, the constitutive equations (4) and (12) remain valid. Now, the growth rate equations for the six damage variables d_{11}^t, d_{11}^c, d_{22}^t, d_{22}^c, d_{12}^+ and d_{12}^- under fully-reversed bending fatigue must be established.

As the shear damage should not depend on the sign of the shear stress, the growth rates $d(d_{12}^+)/dN$ and $d(d_{12}^-)/dN$ are the same. So far, these equations are identical to the equation dD_{12}/dN which was developed for the *multi-dimensional* damage model for *non-reversed cyclic loading* (see Eq. (11)):

$$\begin{cases} \dfrac{d(d_{12}^+)}{dN} = c_1 \cdot \Sigma_{12} \cdot \exp\left(-c_2 \dfrac{d_{12}^+}{2\sqrt{\Sigma_{12}}}\right) & \text{if } \sigma_{12} \geq 0 \\[4mm] \dfrac{d(d_{12}^-)}{dN} = c_1 \cdot \Sigma_{12} \cdot \exp\left(-c_2 \dfrac{d_{12}^-}{2\sqrt{\Sigma_{12}}}\right) & \text{if } \sigma_{12} < 0 \end{cases} \tag{14}$$

To account for the adverse effect of fully-reversed loading, the differential equations $d(d_{12}^+)/dN$ and $d(d_{12}^-)/dN$ are coupled, in a similar way as was done for $d(d_{11}^t)/dN$ and $d(d_{11}^c)/dN$ (see Equation (3)). At each place where the damage d_{11}^t and d_{11}^c appeared as a coupling term in the <u>initiation functions</u> of the one-dimensional model for fully-reversed bending (see Equation (3)), the same function of d_{12}^+ or d_{12}^- has been added to Equation (14) to model the damaging effect of shear reversal:

$$
\begin{cases}
\dfrac{d(d_{12}^+)}{dN} = c_1 \cdot (1+(d_{12}^-)^2) \cdot \Sigma_{12} \cdot \exp\left(-c_2 \dfrac{d_{12}^+}{2\sqrt{\Sigma_{12}} \cdot (1+(d_{12}^-)^2)}\right) & \text{if} \quad \sigma_{12} \geq 0 \\[4mm]
\dfrac{d(d_{12}^-)}{dN} = c_1 \cdot (1+(d_{12}^+)^2) \cdot \Sigma_{12} \cdot \exp\left(-c_2 \dfrac{d_{12}^-}{2\sqrt{\Sigma_{12}} \cdot (1+(d_{12}^+)^2)}\right) & \text{if} \quad \sigma_{12} < 0
\end{cases}
\tag{15}
$$

Regarding the growth rates $d(d_{ii}^t)/dN$ and $d(d_{ii}^c)/dN$ (i = 1,2), two sets of equations can be used:

- Equation (3) of the one-dimensional model provides the expressions for the damage growth rates $d(d_{ii}^t)/dN$ and $d(d_{ii}^c)/dN$ (i = 1,2) under <u>fully-reversed cyclic loading</u>, but <u>without any interaction of shear damage</u>,

- Equation (11) of the multi-axial model provides the expressions for the damage growth rates dD_{11}/dN and dD_{22}/dN under <u>non-reversed cyclic loading</u>, but <u>with interaction of the shear damage D_{12}</u>.

If equations (3) and (11) are combined, the growth rates $d(d_{ii}^t)/dN$ and $d(d_{ii}^c)/dN$ (i = 1,2) can be established. Together with Equation (15), the global system of constitutive equations can be written as (no summation convention):

$$
\begin{cases}
\begin{aligned}
\dfrac{d(d_{ii}^t)}{dN} = \ & c_1 \cdot \left(1+\left(d_{ii}^c\right)^2 + D_{12}^2\right) \cdot \Sigma_{ii} \cdot \exp\left(-c_2 \dfrac{d_{ii}^t}{\sqrt{\Sigma_{ii}} \cdot \left(1+\left(d_{ii}^c\right)^2 + D_{12}^2\right)}\right) \qquad \text{if } \sigma_{ii} \geq 0 \\
& + c_3 \cdot d_{ii}^t \cdot \Sigma_{ii}^2 \cdot \left[1 + \dfrac{\sqrt{d_{ii}^c}\,\exp\!\left(c_8\sqrt{d_{ii}^c}\right)}{1+\exp\!\left(-c_5\left(\Sigma_{ii}-c_7\right)\right)}\right] \cdot \left[1+\exp\!\left(c_5(\Sigma_{ii}-c_4)\right)\right]
\end{aligned} \\[10mm]
\begin{aligned}
\dfrac{d(d_{ii}^c)}{dN} = \ & \left[c_1 \cdot \left(1+\left(d_{ii}^t\right)^2 + D_{12}^2\right) \cdot \Sigma_{ii} \cdot \exp\left(-c_2 \dfrac{d_{ii}^c}{\sqrt{\Sigma_{ii}} \cdot \left(1+\left(d_{ii}^t\right)^2 + D_{12}^2\right)}\right)\right]^{1+2\cdot\exp\left(-c_6\cdot d_{ii}^t - D_{12}\right)} \quad \text{if } \sigma_{ii} < 0 \\
& + c_3 \cdot d_{ii}^c \cdot \Sigma_{ii}^2 \cdot \left[1 + \dfrac{\sqrt{d_{ii}^t}\,\exp\!\left(c_8\sqrt{d_{ii}^t}\right)}{1+\exp\!\left(-c_5\left(\Sigma_{ii}-c_7\right)\right)}\right] \cdot \left[1+\exp\!\left(\dfrac{c_5}{3}(\Sigma_{ii}-c_4)\right)\right]
\end{aligned} \\[10mm]
\dfrac{d(d_{12}^+)}{dN} = c_1 \cdot (1+(d_{12}^-)^2) \cdot \Sigma_{12} \cdot \exp\left(-c_2 \dfrac{d_{12}^+}{2\sqrt{\Sigma_{12}} \cdot (1+(d_{12}^-)^2)}\right) \quad \text{if} \quad \sigma_{12} \geq 0 \\[4mm]
\dfrac{d(d_{12}^-)}{dN} = c_1 \cdot (1+(d_{12}^+)^2) \cdot \Sigma_{12} \cdot \exp\left(-c_2 \dfrac{d_{12}^-}{2\sqrt{\Sigma_{12}} \cdot (1+(d_{12}^+)^2)}\right) \quad \text{if} \quad \sigma_{12} < 0
\end{cases}
\tag{16}
$$

As such, the equations of the *multi-dimensional* model for *fully-reversed cyclic* loading have been established. It is worthwhile to mention that <u>no additional parameters have been included in the model equations (16)</u>, compared to the previous two models. It is also important to observe that the equations (16) for fully-reversed bending reduce to the equations (11) for single-sided bending, if only one damage type is present in each material point.

In the next section, the model will be applied to the fully-reversed bending fatigue tests of [#45°]$_8$ specimens.

FINITE ELEMENT SIMULATIONS

The fatigue model has been applied to the fully-reversed bending test of the [#45°]$_8$ specimen Pr07_4 (u_{max} = 25.5 mm). Figure 6 shows the experimental and simulated results.

Experimental and simulated force-cycle history for [#45°]$_8$ specimen fully-reversed bending, u$_{max}$ = 25.5 mm
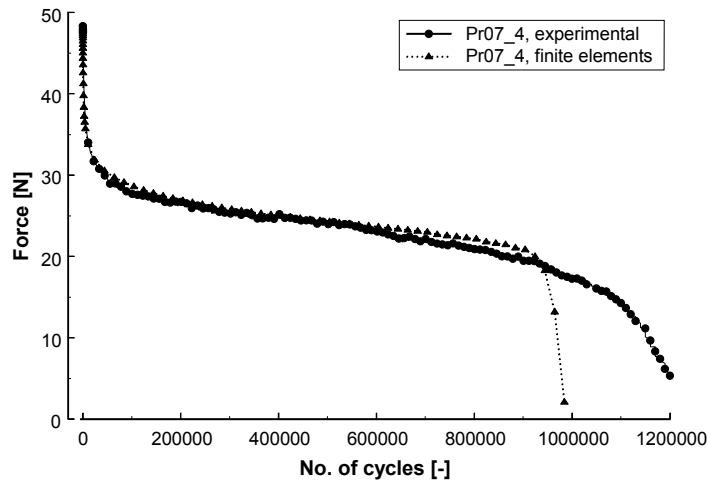
Figure 6   **Experimental and simulated force-cycle history for the [#45°]$_8$ specimen Pr07_4 (u$_{max}$ = 25.5 mm, R$_d$ = -1.0).**

As can be observed from this Figure, the initial decrease of the bending force is very large, almost 20 Newton (if compared with the initial force degradation for the [#45°]$_8$ specimen under single-sided bending in Figure 3). One of the primary reasons for the large force degradation in Figure 6 is the strong coupling effect between D_{12} on the one hand, and D_{11} and D_{22} on the other hand.

To illustrate the importance of the coupling effect, the force-cycle history of the [#45°]$_8$ specimen Pr07_4 has been simulated again, but all coupling terms between D_{12} on the one hand, and D_{11} and D_{22} on the other hand have been removed from Equation (16). As can be seen from Figure 7, the force degradation is seriously underestimated then.

Experimental and simulated force-cycle history for [#45°]₈ specimen fully-reversed bending, u_max = 25.5 mm, no coupling effects
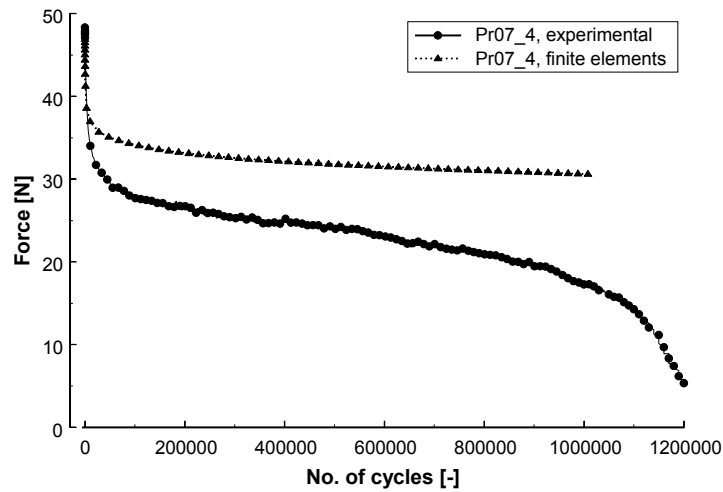

Figure 7   **Experimental and simulated force-cycle history for the [#45°]₈ specimen Pr07_4 (u_max = 25.5 mm, R_d = -1.0) without any coupling effects between D₁₂ on the one hand, and D₁₁ and D₂₂.**

This means that, through the presence of the shear damage D_{12}, the damage variables D_{11} and D_{22} are seriously affected. This can be confirmed by simulating the hypothetic damage state, where the damage D_{12} would be 1.0 in all Gauss-points, but the damage variables D_{11} and D_{22} would be zero, and thus unaffected by the shear damage D_{12}. The corresponding bending force for this hypothetic damage state can be easily calculated through a nonlinear quasi-static analysis with G_{12} being zero for the whole composite specimen (equivalent with $D_{12} = 1.0$ for all Gauss-points), and E_{11} and E_{22} being undamaged. The calculated bending force is then 36.2 N. This means that without any coupling effects, the calculated bending force would still be predicted far too large if compared with the experimentally measured force-cycle history, even if D_{12} would be 1.0 in all Gauss-points. Through the coupling effect between D_{12} on the one hand, and D_{11} and D_{22} on the other hand, the additional decrease of the bending force can be simulated.

Figure 8 shows the simulated cycle history of the damage variables D_{11} $(=d_{11}^t+d_{11}^c)$, D_{22} $(=d_{22}^t+d_{22}^c)$ and D_{12} $(=d_{12}^++d_{12}^-)$ for the Gauss-point 1602, situated at the specimen surface in the clamped cross-section.
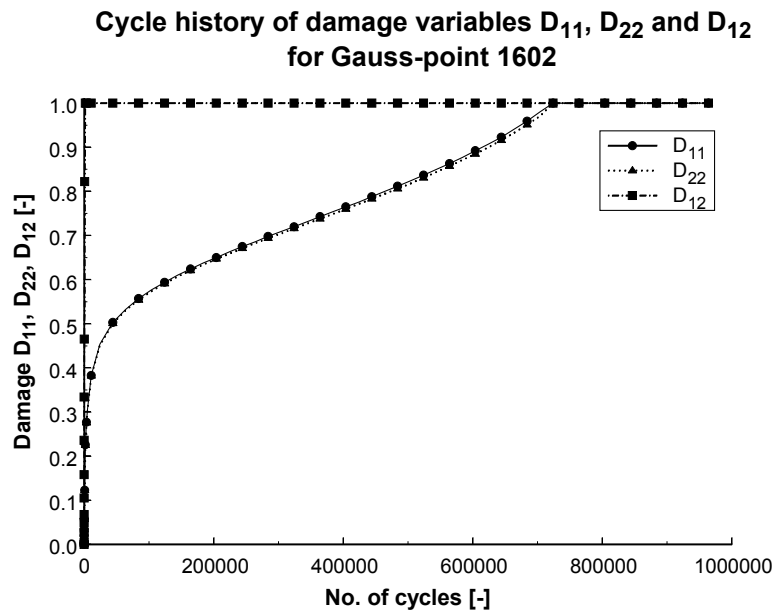
Cycle history of damage variables D_{11}, D_{22} and D_{12} for Gauss-point 1602

Figure 8   **Cycle history of the damage variables D_{11}, D_{22} and D_{12} for the Gauss-point 1602 ([#45°]$_8$ specimen Pr07_4, $u_{max} = 25.5$ mm, $R_d = -1.0$).**

The calculated damage values are much higher than those for the [#45°]$_8$ specimen Pr04_1 (see Figure 4) which was subjected to <u>single-sided bending</u> ($u_{max} = 27.7$ mm). But this is confirmed by the experimentally observed damage patterns for the [#45°]$_8$ specimens Pr04_1 and Pr07_4, as shown in Figure 9. The light areas in the picture represent the damaged parts. In both specimens, the woven fabric reinforcement under 45° with the loading axis can be clearly distinguished. The upper sides of the specimens have been clamped (maximum bending moment), while the displacement has been imposed at the lower sides. The damage pattern at the tensile surface of the [#45°]$_8$ specimen Pr04_1 ($u_{max} = 27.7$ mm, $R_d = 0.0$) is shown at the left. As the [#45°]$_8$ specimen Pr07_4 has been subjected to fully-reversed bending ($u_{max} = 25.5$ mm, $R_d = -1.0$), the damage pattern is the same for both surfaces, and one of the surfaces is shown at the right. It is important to emphasize that the comparision is only qualitative, because the damage variables do not directly represent micromechanical damage mechanisms, but only the perceived effect on the macroscopic elastic properties.
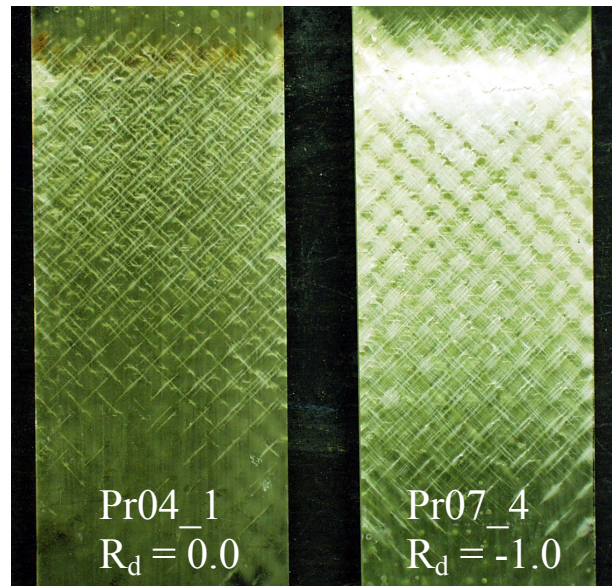
Figure 9   **Damage pattern at the tensile surface of the Pr04_1 specimen (left) (u_{max} = 27.7 mm, R_d = 0.0), and damage pattern at the surface of the Pr07_4 specimen (right) (u_{max} = 25.5 mm, R_d = -1.0).**

Finally, Figure 10 shows the experimental and simulated force-cycle history for the $[\#45°]_8$ specimen Pr07_1, which has been subjected to fully-reversed bending for u_{max} = 19.5 mm. Of course all material constants c_i (i=1,...,9) have retained their same values.
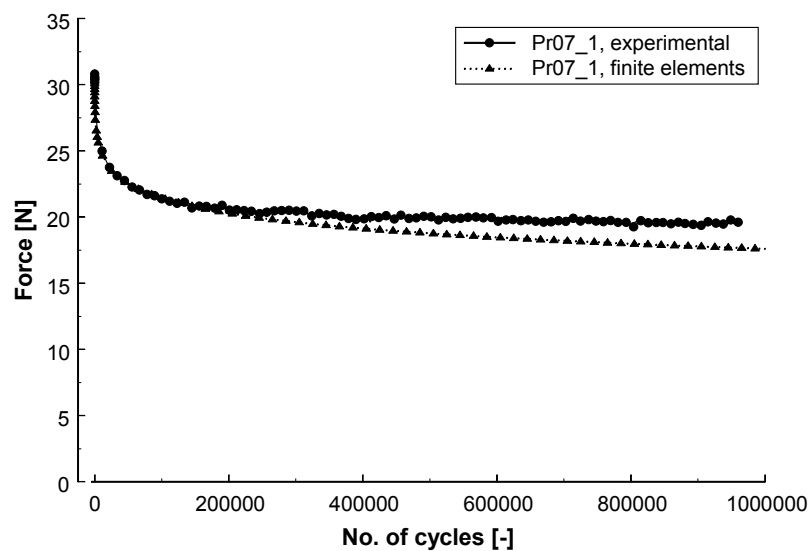

Figure 10   **Experimental and simulated force-cycle history for the $[\#45°]_8$ specimen Pr07_1 (u_{max} = 19.5 mm, R_d = -1.0).**

Although the initial force is much smaller (F = 30.8 N) than for the Pr07_4 specimen, the initial decline is simulated very well. It appears however that the damage propagation is somewhat overpredicted by the fatigue damage model. This proves that the value of the threshold for damage propagation is subject to some experimental scatter, but this is an intrinsic property of fatigue experiments.

CONCLUSIONS

Previous work of the authors resulted in a *one-dimensional* damage model for *fully-reversed cyclic loading* and a *multi-dimensional* damage model for *non-reversed cyclic loading*. In this paper, features of both models have been integrated into a *multi-dimensional* model for *fully-reversed cyclic loading.*

For this latter damage model, six damage variables d_{11}^t, d_{11}^c, d_{22}^t, d_{22}^c, d_{12}^+ and d_{12}^- have been introduced that affect the inplane elastic properties of the orthotropic composite material. The damage-stiffness relationships are quite straightforward, because the damage variables are each directly related with their corresponding stress components σ_{11}, σ_{22} and σ_{12}. If the damage variables would represent the actual fatigue damage mechanisms, the development of the damage-stiffness relationships would be far more complicated, because it would be very difficult to examine experimentally in what manner the individual fatigue damage mechanisms affect the various elastic properties. Moreover, the growth rate equations for certain fatigue damage mechanisms would be driven in particular by the matrix or fibre stress (not to mention the influence of its maximum stress amplitude and stress ratio). For the present fatigue damage model, interaction between different damage modes is still possible by coupling the differential growth rate equations (as was done for fully-reversed loading and the effect of shear damage), but these interactions are kept at the level of the damage growth rate equations. For the higher level of the damage-stiffness relationships, the non-diagonal elements of the damage matrix are zero and no explicit coupling is done.

The constitutive stress-strain relations and the damage growth rate equations have been implemented in a commercial finite element code and adaptive time stepping has been applied to simulate the successive damage states during fatigue loading. Finite element simulations have proven that reliable simulations can be done and that the evolution of the damage state variables, inplane stresses and stiffness degradation can be simulated. Although it is not claimed that the presented model is valid for other fibre architectures and more fibre dominated fatigue loadings, the authors believe that the general modelling framework can remain useful and that the damage growth rate equations and its material constants can be optimized for other composite materials under study.

ACKNOWLEDGEMENTS

REFERENCES

Van Paepegem, W. and Degrieck, J. (2004). Simulating in-plane fatigue damage in woven glass fibre-reinforced composites subject to fully-reversed cyclic loading. *Fatigue and Fracture of Engineering Materials & Structures*, 27(12), 1197-1208

[1]   Bartley-Cho, J., Lim, S.G., Hahn, H.T. and Shyprykevich, P. (1998). Damage accumulation in quasi-isotropic graphite/epoxy laminates under constant-amplitude fatigue and block loading. Composites Science and Technology, 58, 1535-1547.

[2]   Gathercole, N., Reiter, H., Adam, T. and Harris, B. (1994). Life prediction for fatigue of T800/5245 carbon-fibre composites: I. Constant-amplitude loading. International Journal of Fatigue, 16(8), 523-532.

[3]   Adam, T., Gathercole, N., Reiter, H. and Harris, B. (1994). Life prediction for fatigue of T800/5245 carbon-fibre composites: II. Variable-amplitude loading. International Journal of Fatigue, 16(8), 533-547.

[4]   Badaliance, R., Dill, H.D. and Potter, J.M. (1982). Effects of spectrum variations on fatigue life of composites. In : Daniel, I.M. (ed.). Composite materials : Testing and design (Sixth Conference). ASTM STP 787. Philadelphia, American Society for Testing and Materials, pp. 274-286.

[5]   Gamstedt, E.K. and Sjogren, B.A. (1999). Micromechanisms in tension-compression fatigue of composite laminates containing transverse plies. Composites Science and Technology, 59(2), 167-178.

[6]   Curtis, P.T. (1989). The fatigue of organic matrix composite materials. In : Partridge, I.K. (ed.). Advanced composites. Londen, Elsevier, pp. 331-367.

[7]   Van Paepegem, W. and Degrieck, J. (2002). Tensile and Compressive Damage Coupling for Fully-reversed Bending Fatigue of Fibre-reinforced Composites. Fatigue and Fracture of Engineering Materials & Structures, 25(6), 547-562.

[8]   Kachanov, L.M. (1958). On creep rupture time. Izv. Acad. Nauk SSSR, Otd. Techn. Nauk, No.8, 26-31.

[9]   Kachanov, L.M. (1986). Introduction to continuum damage mechanics. Dordrecht, Martinus Nijhoff Publishers, 135 pp.

[10]   Krajcinovic, D. and Lemaitre, J. (eds.) (1987). Continuum damage mechanics: theory and applications. Wien, Springer - Verlag, 294 pp.

[11]   Chaboche, J.L. (1988). Continuum damage mechanics : part I - General concepts. Journal of Applied Mechanics, 55, 59-64.

[12]   Chaboche, J.L. (1988). Continuum damage mechanics : part II - Damage growth, crack initiation and crack growth. Journal of Applied Mechanics, 55, 65-72.

[13]   Krajcinovic, D. (1985). Continuous damage mechanics revisited : basic concepts and definitions. Journal of Applied Mechanics, 52, 829-834.

[14]   Sidoroff, F. (1984). Damage mechanics and its application to composite materials. In : Cardon, A.H. and Verchery, G. (eds.). Mechanical characterisation of load bearing fibre composite laminates. Proceedings of the European Mechanics Colloquium 182, 29-31 August 1984, Brussels, Belgium, Elsevier, pp. 21-35.

[15]   O'Brien, T.K. and Reifsnider, K.L. (1981). Fatigue damage evaluation through stiffness measurements in boron-epoxy laminates. Journal of Composite Materials, 15, 55-70.

[16]   Highsmith, A.L. and Reifsnider, K.L. (1982). Stiffness-reduction mechanisms in composite laminates. In : Reifsnider, K.L. (ed.). Damage in composite materials. ASTM STP 775. American Society for Testing and Materials, pp. 103-117.

[17]   Reifsnider, K.L. (1987). Life prediction analysis : directions and divagations. In : Matthews, F.L., Buskell, N.C.R., Hodgkinson, J.M. and Morton, J. (eds.). Sixth International Conference on Composite Materials (ICCM-VI) & Second European Conference on Composite Materials (ECCM-II) : Volume 4. Proceedings, 20-24 July 1987, London, UK, Elsevier, pp. 4.1-4.31.

[18]   Van Paepegem, W. and Degrieck, J. (2002). A New Coupled Approach of Residual Stiffness and Strength for Fatigue of Fibre-reinforced Composites. International Journal of Fatigue, 24(7), 747-762.

[19]   Fujii, T., Amijima, S. and Okubo, K. (1993). Microscopic fatigue processes in a plain-weave glass-fibre composite. Composites Science and Technology, 49, 327-333.

[20]   Schulte, K., Reese, E. and Chou, T.-W. (1987). Fatigue behaviour and damage development in woven fabric and hybrid fabric composites. In : Matthews, F.L., Buskell, N.C.R., Hodgkinson, J.M. and Morton, J. (eds.). Sixth International Conference on Composite Materials (ICCM-VI) & Second European Conference on Composite Materials (ECCM-II) : Volume 4. Proceedings, 20-24 July 1987, London, UK, Elsevier, pp. 4.89-4.99.

[21]   Hansen, U. (1997). Damage development in woven fabric composites during tension-tension fatigue. In : Andersen, S.I., Brøndsted, P., Lilholt, H., Lystrup, Aa., Rheinländer, J.T., Sørensen, B.F. and Toftegaard, H. (eds.). Polymeric Composites - Expanding the Limits. Proceedings of the 18th Risø International Symposium on Materials Science, 1-5 September 1997, Roskilde, Denmark, Risø International Laboratory, pp. 345-351.

[22]   Ferry, L., Gabory, D., Sicot, N., Berard, J.Y., Perreux, D. and Varchon, D. (1997). Experimental study of glass-epoxy composite bars loaded in combined bending and torsion loads. Fatigue and

characterisation of the damage growth. In : Degallaix, S., Bathias, C. and Fougères, R. (eds.). International Conference on fatigue of composites. Proceedings, 3-5 June 1997, Paris, France, La Société Française de Métallurgie et de Matériaux, pp. 266-273.

[23] Herrington, P.D. and Doucet, A.B. (1992). Progression of bending fatigue damage around a discontinuity in glass/epoxy composites. Journal of Composite Materials, 26(14), 2045-2059.

[24] Chen, A.S. and Matthews, F.L. (1993). Biaxial flexural fatigue of composite plates. In : Miravete, A. (ed.). ICCM/9 Composites : properties and applications. Volume VI. Proceedings of the Ninth International Conference on Composite Materials, 12-16 July 1993, Madrid, Spain, Woodhead Publishing Limited, pp. 899-906.

[25] Lemaitre, J. (1971). Evaluation of dissipation and damage in metals, submitted to dynamic loading. Proceedings I.C.M. I, Kyoto, Japan.

[26] Van Paepegem, W. and Degrieck, J. (2002). Coupled Residual Stiffness and Strength Model for Fatigue of Fibre-reinforced Composite Materials. Composites Science and Technology, 62(5), 687-696.

[27] Van Paepegem, W. and Degrieck, J. (2003). Modelling damage and permanent strain in fibre-reinforced composites under in-plane fatigue loading. Composites Science and Technology, 63(5), 677-694.

[28] Van Paepegem, W. (2002). Development and finite element implementation of a damage model for fatigue of fibre-reinforced polymers. Ph.D. thesis. Gent, Belgium, Ghent University Architectural and Engineering Press (ISBN 90-76714-13-4), 403 p.

[29] Van Paepegem, W. and Degrieck, J. (2003). Calculation of Damage-dependent Directional Failure Indices from the Tsai-Wu Static Failure Criterion. Composites Science and Technology, 63(2), 305-310.